

---

# DBSEGMENT: FAST AND ROBUST SEGMENTATION OF DEEP BRAIN STRUCTURES - EVALUATION OF TRANSPORTABILITY ACROSS ACQUISITION DOMAINS

---

**Mehri Baniasadi,**

Luxembourg Center for Systems Biomedicine,  
University of Luxembourg,  
National Department of Neurosurgery,  
Centre Hospitalier de Luxembourg,  
mehri.baniasadi@uni.lu,

**Mikkel V. Petersen,**

Department of Clinical Medicine,  
Center of Functionally Integrative Neuroscience,  
University of Aarhus,

**Jorge Gonçalves,**

Luxembourg Center for Systems Biomedicine,  
University of Luxembourg,

**Andreas Horn,**

Neuromodulation and Movement Disorders Unit,  
Department of Neurology,  
Charité – Universitätsmedizin Berlin,

**Vanja Vlasov,**

Luxembourg Center for Systems Biomedicine,  
University of Luxembourg,

**Frank Hertel,**

National Department of Neurosurgery,  
Centre Hospitalier de Luxembourg,

**Andreas Husch,**

Luxembourg Center for Systems Biomedicine,  
University of Luxembourg,

## ABSTRACT

Segmenting deep brain structures from magnetic resonance images is important for patient diagnosis, surgical planning, and research. Most current state-of-the-art solutions follow a segmentation-by-registration approach, where subject MRIs are mapped to a template with well-defined segmentations. However, registration-based pipelines are time consuming, thus, limiting their clinical use. This paper uses deep learning to provide a one-step, robust and efficient deep brain segmentation solution directly in the patient's native space. The method consists of a pre-processing step to conform all MRI images to the same orientation, followed by a convolutional neural network using the nnU-Net framework. We use a total of 14 datasets from both research and clinical collections. Of these, seven were used for training and validation and seven were retained for independent testing. We trained the network to segment 30 deep brain structures, as well as a brain mask, using labels generated from a registration-based approach. We evaluated the generalizability of the network by performing a leave-one-dataset-out cross-validation, and extensive testing on unseen datasets. Furthermore, we assessed cross-domain transportability by evaluating the results separately on different domains. We achieved an average dice score similarity of  $0.89 \pm 0.04$  on the test datasets when compared to the registration-based gold-standard. On our test system, the computation time decreased from 43 minutes for a reference registration-based pipeline to 1.3 minute. Our proposed method is fast, robust, and generalizes with high reliability. It can be extended to the segmentation of other brain structures. The method is publicly available on GitHub, as well as a pip package for convenient usage.

**Keywords** Segmentation · Deep Brain Structures · Deep Learning · MRI · Confounder

# 1 Introduction

Segmentation of deep brain nuclei from structural Magnetic Resonance Imaging (MRI) data is widely-used in clinical practice and in research [1, 2]. Segmentation allows localisation of structures and extraction of morphological features, relevant for diagnosis, treatment planning, and disease follow-up [3, 4]. For example, in Parkinson’s Disease (PD), where patients show characteristic morphological changes of the Substantia nigra (SN), segmentation of this region and other basal ganglia nuclei has been important in studying disease progression. Furthermore, accurate segmentation processes are of value for identifying diagnostic biomarkers that can help differentiate PD from other parkinsonian syndromes [5, 6].

Another important application is pre-operative planning and post-operative evaluation of Deep Brain Stimulation (DBS) surgery [7, 8, 9]. DBS is an established treatment for movement disorders and psychiatric diseases, in which the target, a specific deep brain structure, is stimulated via an implanted electrode [10, 11, 12, 13]. DBS target structures cannot be clearly visualized during the intervention and therefore, pre-operative localisation of the target structure is important for the surgical targeting [14]. Precise planning is necessary for accurate placement of the DBS electrodes, and results in a better treatment outcome [15]. After surgery, the device settings, such as stimulation amplitude, and the active contacts of the implanted electrode, are systematically tested during a programming session [16]. The goal of this session is to find optimal settings that stimulate the target region, while avoiding regions that cause side-effects. A detailed understanding of the spatial relationship between target structure, region of avoidance, and the implanted electrode, can provide valuable information for the time-consuming process of fine-tuning stimulation parameters [17, 18, 19].

## 1.1 Segmentation by registration

For brain structure segmentation, the most used method is registration-based, also called atlas-based registration [20], using an atlas containing labelled segmentations in a specific template imaging-space. The reference template data is typically an averaged T1-weighted (T1w) image such as Montreal Neurological Institute (*MNI*), *Deepbrain7T*, or the California Institute of Technology (*CIT168*) template [21, 22, 23, 24]. This method is typically multi-stage, including pre-registration steps, such as bias field correction and skull stripping, followed by multiple registration stages, with increasing degrees of freedom as the registration advances [25, 26]. The subject’s image is registered to the template, and the atlas (e.g. Distal, THOMAS, and the CIT168 atlas, etc.) is used to map the location of the labelled brain structures [27, 28, 24]. The final output is structural segmentation maps generated in the the subject-specific-image-space. Multispectral approaches that include other sequences beyond T1 have been shown to lead to better results [27]. Popular registration tools include Advanced Normalization Tool (ANTs <sup>1</sup>), FMRIB Software Library (FSL <sup>2</sup>), Statistical parametric mapping (SPM <sup>3</sup>), and Deformable registration via attribute matching and mutual-saliency weighting (DRAMMS) [29, 30, 31, 32, 33, 34, 35, 36].

The accuracy of the segmentation can be impacted by pre-processing steps, registration method and algorithm parameter selection [26]. A number of studies have addressed the challenge of segmentation accuracy, and have proposed registration-based pipelines for brain structure segmentation [25, 37]. For example, Schönecker et al proposed an automated pipeline for linear registration of subject images to MNI space using FSL tools. Skull-stripped images, registered to MNI space with an affine transformation, are refined further in a multi-stage process using first a subcortical mask extended to cover potential enlarged ventricles, and second a smaller stereotactic mask, covering the basal ganglia [38]. DBS Auto Report (DBSAR) is another automatic pipeline that maps basal ganglia structures from the Deep7T atlas to the subject’s image. It is based on a multi-stage ANTs registration pipeline [39]. Another example of a tool integrating multiple registration approaches is Lead-DBS, a DBS-focused toolbox that provides a user-interface to perform each registration step with user-selected method. This toolbox supports a large number of well established registration algorithms [40, 41].

In multi-stage registration pipelines, errors can occur at different stages and lead to incorrect or inaccurate segmentation maps. During the registration process, the subject’s image is mapped to the reference template image. Cases where there are significant differences between subject and template images can especially challenge the registration process. In clinical settings, this can present a significant challenge, for example if a patient’s image has a reduced field of view (a partial brain), or in the case of head tilting during the image acquisition [42]. Furthermore, the registration process includes optimization steps and is computationally demanding, especially in the case of a multi-atlas registration. Therefore, there is a clear need for computationally less demanding methods, for clinical use, or indeed for large cohort studies. [43, 21, 44].

---

<sup>1</sup><http://stnava.github.io/ANTs/>

<sup>2</sup><https://fsl.fmrib.ox.ac.uk/fsl/fslwiki/FLIRT>

<sup>3</sup><https://www.fil.ion.ucl.ac.uk/spm/software/spm12/>

## 1.2 Deep learning based segmentation

Supervised deep learning approaches are an alternative for brain structures segmentation [45]. Several existing studies have proposed segmentation of brain structures using convolutional neural networks (CNN) [46, 47, 48]. For example, Quick Segmentation of NeuroAnaTomy (QuickNAT) segments the whole brain into 27 structures. It consists of three 2D fully CNNs (F-CNNs) for the axial, coronal, and sagittal planes. During the inference, the three orthographic planes are aggregated. The F-CNNs have U-Net architecture with unpooling layers, and dense connections [49]. FastSurfer segments the brain into 95 regions. Similar to QuickNAT, it consists of three 2D F-CNNs for the three orthographic planes followed by a view aggregation step. The F-CNNs have U-Net architecture with competitive dense blocks, multi-slice information, and competitive skip pathways [44]. However, these methods focus on the segmentation of large brain structures and do not include smaller deep brain structures.

Hough-CNN, proposed a method for segmenting 26 deep brain structures, where the second last fully connected layer of the CNN is used to localize and segment the structures[2]. The method was tested and evaluated on 26 subjects (122 volumes). However, performance was poor when compared to the methods using U-Net architecture, the current state-of-the-art for segmentation. A publication called M-net, proposed a network for segmenting 14 structures using a 2D-U-Net architecture [50]. This method was tested on two datasets, International Brain Segmentation Repository (IBSR) with 18 subjects, and MICCAI 2013 SATA challenge, with 35 subjects for training and 12 for testing . Rashed et al. proposed a method for segmenting 7 deep brain structures using a single-encoder, and multi-decoder CNN [51]. The method was evaluated on two datasets, NAMIC (Brain Multimodality) dataset with 18 subjects and the MICCAI 2012 workshop dataset with 35 subjects. However, for all of these methods [2, 50, 51], no testing on unseen datasets or validations were performed, which is an important step to ensure generalizability to unseen data. To us, this was of particular importance, considering the high degree of variability in MRI data from different datasets.

## 1.3 Our proposed method

In this study, We propose a novel and rapid deep learning approach to segment 30 deep brain structures from T1w MRI (Figure 1).The method consists of a pre-processing step to transform all the images to the same reference orientation followed by nnU-Net framework for segmentation [52], and finally, transformation back to the native space, all in one step. The pre-processing helps the network to generalize even on the datasets where nnU-Net fails [52].

We test our fully automated method, using data from both research-oriented and clinical acquisitions, with imaging data from different scanners, sequence protocols, age range, subject health, and sex. We compared our approach to a multi-stage registration-based method. We evaluate the generalisability of the network by performing a leave-one-dataset-out (LODO) cross-validation, and extensive testing on diverse unseen datasets. Finally, we perform an ablation to evaluate the cross-domain transportability. In this work we focus on the small deep brain structures, such as Ventral intermediate thalamic nucleus (VIM), Ventral posterolateral nucleus of thalamus (VPL) and the Habenular Nuclei (HN), which have not been the focus of previous methods development.

## 2 Methods

We segment 30 deep brain structures from T1w MRIs with a deep learning-based method using the nnU-Net platform [52]. We used a large and diverse dataset, annotated using a registration-based method. Our method involves an essential pre-processing to conform all MR images to the same orientation, voxel spacing, and dimension, before the network training. We trained and evaluated the network with the LODO cross-validation, and performed testing on several unseen datasets. Additionally, we performed an ablation study by separating results into different domains based on the factors affecting the segmentation performance. This was done to evaluate the cross-domain transportability. Finally, we performed another ablation study to emphasize the importance of the pre-processing steps.

### 2.1 Datasets

We used data from 10 public datasets together with 4 anonymized datasets from clinical centers for training and testing. The following datasets were used for training and LODO cross-validation, the Human connectome project’s young adults, HCP <sup>4</sup> [53], Autism Brain data exchange II, ABIDE II <sup>5</sup> [54], Parkinson’s Progression Markers Initiative, PPMI

---

<sup>4</sup><http://www.humanconnectomeproject.org/>

<sup>5</sup>[http://fcon\\_1000.projects.nitrc.org/indi/abide/abide\\_II.html](http://fcon_1000.projects.nitrc.org/indi/abide/abide_II.html)

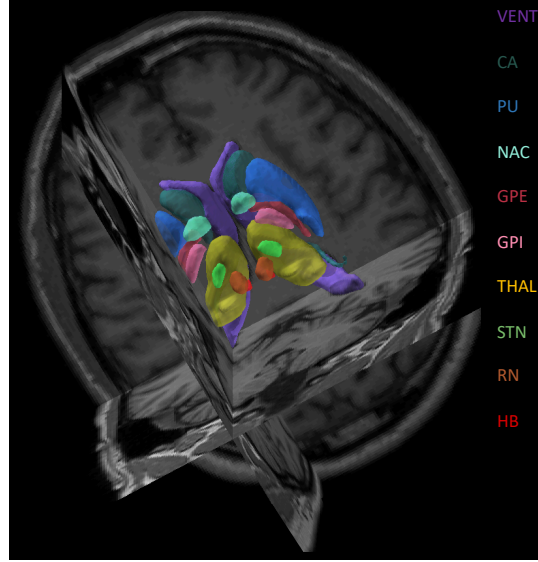


Figure 1: **Deep brain structures segmentation.** The segmentation results of the network is shown for one of the test scans. The right and the left hemisphere are visualized with the same color. SNC, SNR, VIM, and VPL are not shown in this figure. The full name of the structures can be found in table S3.

<sup>6</sup> [55], Alzheimer’s disease Neuroimaging Initiative, ADNI <sup>7</sup> [56], Open Access Series of Imaging Studies 3, OASIS3 <sup>8</sup> [57], Minimal Interval resonance Imaging in Alzheimer’s Disease, MIRIAD <sup>9</sup> [58], and deidentified MRIs of Epilepsy patients from Shanghai Ruijin Hospital, SRH (clinical). The method is validated using data from unseen datasets (test sets), including, Information eXchange from Images, IXI <sup>10</sup>, the UCLA Consortium for Neuropsychiatric Phenomics, LA5c <sup>11</sup>, obtained from the OpenfMRI database, with accession number of ds000030 [59], Designed Database of MR Brain Images of Healthy Volunteers from the University of North Carolina, UNC <sup>12</sup> [60], Designed Database of MR brain images of Healthy Volunteers, Travelling Human phantom, THP <sup>13</sup> [61], and deidentified data of the DBS patients from the Centre Hospitalier de Luxembourg, CHL (clinical), Charité Universitätsmedizin Berlin, CUB (clinical), and Aarhus University Hospital in Denmark, AUH (clinical). We collected a diverse dataset, including images from various scanners, with different acquisition protocols, and intensity ranges. The data contains healthy subjects and patients with neurological and psychiatric disorders across a wide range of age. The Maximum number of subjects used from one dataset is 100 (randomly selected), to avoid overfitting to one specific dataset. All datasets except THP, contain only a single scan from each subject. Detailed information about the training, and test data can be found in Table 1.

## 2.2 Pre-processing

All MR images in this study were resampled to  $1 \times 1 \times 1$  mm voxel spacing,  $256 \times 256 \times 256$  dimensions, and conformed to the same slice orientation, Left-Posterior-Inferior (LPI) [44]. Additionally, all the default nnU-Net pre-processing steps, such as data augmentation, and intensity normalization, were applied before any training.

## 2.3 Data annotation

We created a label file including the segmentation of the 30 selected brain structures in MNI space (ICBM 2009b Nonlinear Asymmetric) [22]. This label file is generated once, later, when we get the transformation matrix from the native space to the MNI space for each subject, we transform this label file to the native space of that subject.

<sup>6</sup>[www.ppmi-info.org](http://www.ppmi-info.org)

<sup>7</sup><http://adni.loni.usc.edu/>

<sup>8</sup><https://www.oasis-brains.org/>

<sup>9</sup><http://miriad.drc.ion.ucl.ac.uk/>

<sup>10</sup><https://brain-development.org/ixi-dataset/>

<sup>11</sup><https://openfmri.org/dataset/ds000030/>

<sup>12</sup><https://www.insight-journal.org/midas/community/view/21>

<sup>13</sup><https://openneuro.org/datasets/ds000206/versions/1.0.0>



Usage	Dataset	Scanner	1.5T/3T	Protocol	Gado	Disease	Origin	Age	#
Training and Cross Validation	HCP	SM	3T	MPRAGE	N	HT	RS	22-35	100
	OASIS3	SM	3T	MPRAGE	N	HT, AD, DM	RS	49-87	100
	ADNI	GE, SM, PL	1.5T, 3T	MPRAGE	N	HT, AD, MC, CI	RS	57-90	100
Cross Validation	PPMI	GE, SM, PL	1.5T, 3T	MPRAGE, FSPGR	N	HT, PD, ESP, HT	RS	31-83	100
	ABIDE-II	PL	3T	MPRGAE, FSPGR	N	HT, AT	RS	5-64	100
	MIRIAD	GE	1.5T	FSPGR	N	HT, PD	RS	55-80	64
	SRH	N/A	N/A	N/A	Y/N	EP	CL	N/A	42
External Test	IXI	GE, PL	1.5T, 3T	N/A	N	HT	RS	20-86	100
	LA5C	SM	3T	MPRGAE	N	HT, BP, SZ, AHD	RS	21-50	100
	UNC	SM	3T	MPRAGE, FLASH	N	HT	RS	22-68	100
	THP	SM, PL	3T	MPRGAE	N	HT	RS	N/A	45
	CHL	GE, SM	3T	FSPGR	Y/N	PD, ET, DT, PN	CL	44-70	25
	CUB	SM	N/A	MPRAGE	Y/N	PD	CL	37-73	39
	AUH	SM	3T	MPRGAE	N	PD	CL	58 ± 6	13

Table 1: **The meta data of the training and the test set.** 7 datasets are used for the training and the leave one dataset out cross-validation, and the other 7 datasets are used for testing. Three types of scanners are used for image acquisition, Siemens (SM), Philips (PL), and General Electric (GE). Among them, there are 1.5 and 3 Tesla (T) scanners. A wide range of protocols were used for the image acquisition and can be categorized into three groups; MPRAGE, FSPGR, and FLASH. In some scans, gadolinium enhancement (Gado) was used. This is shown by Yes (Y), if the gadolinium enhancement was performed otherwise No (N). The HCP datasets contains Healthy (HT) subjects, OASIS3: HT, Alzheimer’s Disease (AD), and Dementia (DT), ADNI: HT, AD, Memory Concern (MC), and Cognitive Impairment (CI), PPMI: HT, Parkinson’s Disease (PD), and Prodromal (Early Stage Parkinson’s disease - ESP), ABIDE-II: HT, and Autism (AT), MIRIAD: HT, and AD, SRH: Epilepsy (EP), IXI: HT, LA5C: HT, Bipolar disorder (BP), Schizophrenia (SZ), and Attention deficit Hyperactivity Disorder (AHD), UNC: HT, THP: HT, CHL: PD, Essential Tremor (ET), Dystonia (DT), Pain (PN), CUB: PD, AUH: PD. Some of the datasets are downloaded from open source servers and are generated for a specific research project. We refer to them as research-orientated datasets (Research-RS). Other datasets are collected from our clinical collaborators and we refer to them as clinical or CL. The age range of subjects used in this study are shown in the Age column, and finally the number (#) of data used from each dataset are shown in the last column. N/A means that the corresponding meta data was not available.

The segmentation maps were combined from the CIT168, DISTAL, and THOMAS atlases [27, 28, 24]. Each structure was initially resampled to the MNI space, and thresholded at 0.5 to generate a binary label. The lateral ventricles were manually segmented using the MNI template in the ITK-SNAP toolbox<sup>14</sup> [62]. The segmentation labels were combined into a single file, in which each structure has a corresponding index. The full name of the labels, and their origin are outlined in Table S3.

The subject T1w images were annotated with the generated label file using the atlas-based method described in [39]. In brief, we first applied N4-bias field correction and skull stripping. Next, we used ANTs to calculate a non-linear warp between the subject T1w image and the MNI reference image. Using this transformation we warped the segmentation labels to the subject image, resulting in segmentation of the 30 brain structures in the subject’s native image space. Additionally, we used ANTs to generate a whole brain mask. This brain mask was added to the 30 segmentation labels to improve the network performance by helping it locate the brain area. All the images were randomly selected from the original datasets. All the registrations were checked to ensure the results. If the registration pipeline failed on a subject and the generated segmentation labels were fully incorrect, then the subject’s image was discarded, to avoid any incorrect training by the network.

## 2.4 LODO cross-validation and testing

We used the nnU-Net framework for the training [52]. The network is a U-Net composed of an encoder-decoder architecture with skip connections. We trained a 3D full resolution network with the batch size of 2 and patch size of [128 128 112]. The optimizer is Stochastic gradient descent with Nesterov momentum ( $\mu = 0.99$ ). nnU-Net performs a random 5-fold cross-validation during the training. For this study, we did not train the network with the default cross-validation of nnU-Net, instead, we performed a LODO cross-validation. This was done to evaluate the generalizability of the network and cross-dataset transportability. We trained 7 different networks (7 folds), during the training. All subjects from one dataset were left out while subjects from the 6 other datasets were used for the training. The performance of the network was evaluated on the dataset that was left out. The procedure was repeated for all 7 networks. Lastly, we ensembled all the folds to generate the final network. Any combination of the 7 folds is possible.

<sup>14</sup>[www.itk-snap.org](http://www.itk-snap.org)

Selecting fewer folds will directly reduce computation time. In practice, two folds are sufficient to cover all the training data. We evaluated the performance of the final ensemble model (all folds) on 7 unseen datasets (Test set).

## 2.5 Evaluation metrics

We evaluated the performance of the network using the Dice similarity coefficient (DSC) and the average Hausdorff distance (AHD).

DSC is a widely used metric to evaluate the similarity between two segmentation tasks. Here, we compared the segmentations generated with our network with the registration-based segmentation method (gold standard). We measured the DSC separately for each structure, considering the value of 1 for the structure and 0 for the rest of the image. Average DSC per subject is the average DSC of all its structures excluding the brain mask.

Hausdorff distance is a metric to evaluate the longest distance between two sets of points. In the field of segmentation, it is used to compare the boundaries of two segmentation tasks. For this purpose, we measured the average Hausdorff distance (AHD) using SimpleITK Python Toolkit<sup>15</sup>. Similar to the DSC, we measured the AHD for each structure separately.

$$DS(G, P) = \frac{2|G \cap P|}{|G| + |P|} \quad (1)$$

Hausdorff distance is a metric to evaluate the longest distance between two sets of points. In the field of segmentation, it is used to compare the boundaries of two segmentation tasks. For this purpose, we measured the AHD, which is defined as

$$AHD(G, P) = \frac{1}{|G|} \sum_{g \in G} \min_{p \in P} (g, p) + \frac{1}{|P|} \sum_{p \in P} \min_{g \in G} (p, g) \quad (2)$$

$|G|$ , and  $|P|$  are the sets of points in the gold standard and network prediction respectively. Similar to the DSC, we measured the AVG HD for each structure separately [63].

## 2.6 Causal diagram

To address the question of why the DSC is lower in some data compared to the others, we decided to draw a causal diagram for our study. 2.

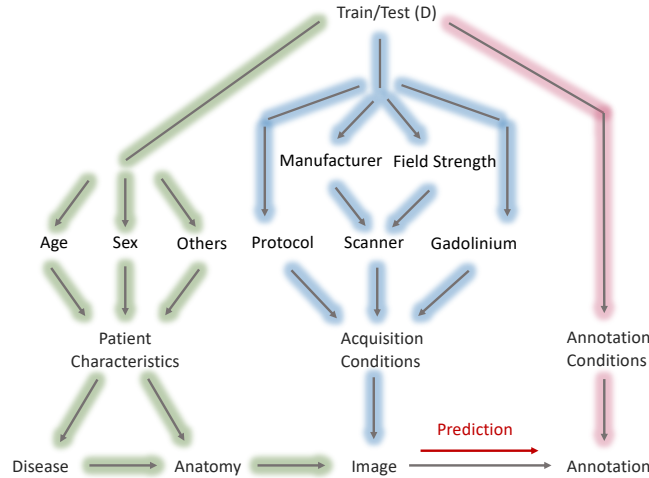


Figure 2: The causal diagram of the deep brain structures segmentation workflow.

This diagram is inspired by the scaffold causal diagram suggested by [64] for medical imaging workflows. We expanded the original diagram by adding factors affecting acquisition conditions such as scanner (manufacturer, field strength),

<sup>15</sup><https://simpleitk.org/>

acquisition protocol, and the use of gadolinium. In addition, we expanded the patient characteristics by including factors such as age and sex. Due to the limited meta data, we did not examine other factors such as ethnicity, handedness etc. Our gold standard annotation (segmentation) was obtained by the registration-based approach using ANTs. Any change in the image caused by other factors of the diagram, can affect the performance of ANTs, as well. However, to simplify the graph, we did not include any factor in annotation conditions for this study.

We used this diagram to extract the factors affecting the final annotation, as well as an ablation study to evaluate the effect of each factor on the final DSC. For each factor, we separated all the cross-validation and test results into different classes. For instance, one of the factors affecting the annotation is the acquisition protocol. In this case, we separated the validation data into 3 protocol domains, including MPRAGE, FSPGR, and FLASH. This was to see if the performance on one domain differs compared to the others. We also measured the prevalence of each class in the training and test datasets to evaluate the existence of acquisition shift.

## 2.7 Gadolinium star

Gadolinium contrast agent enhancement is a technique used in the radiology to increase the contrast of perfused tissue. A solution of gadolinium contrast agent is injected to the patient before image acquisition. This technique alters the relaxation time of certain tissues, and lead to increased contrast between vessels and surrounding brain tissue [65]. To examine the impact of the increased vessel contrast on the segmentation task, we reduced the vessel intensities to synthetically generate a non-gadolinium scan (scans with no gadolinium enhancement) from a gadolinium scan (scans with gadolinium enhancement). This was done to compare the accuracy of the segmentation on both gadolinium and non-gadolinium scan of the same subject. We refer to the synthetically generated scan, as gadolinium star (gadolinium\*). The gadolinium\* scans were generated automatically using ITK-SNAP and FSL. We extracted the brain area of the scan using the brainmask. Next, We thresholded the part of the brain with intensities higher than 65% of the whole intensity range. We scaled the thresholded part to a negative value (-0.4) and added the the scaled thresholded region back to the original image. Finally we smoothed it with a sphere kernel with the radius of 1mm.

## 2.8 Pre-processing ablation study

In the ablation study, we evaluated the necessity of each pre-processing step. For this, we trained one network with no pre-processing, and four networks with different pre-processing steps, here referred to as pre-processing versions 1 to 4. In version 1, we perform only one pre-processing step, conforming all images to the same orientation, LPI. In version 2, we add one more step and conform all the images to the same orientation and voxel spacing ( $1 \times 1 \times 1$  mm). In version 3, we conform all images to the same orientation, voxel spacing, and dimension ( $256 \times 256 \times 256$ ). In version 4 we additionally normalize all images to the same intensity range (0-255). The last step is done only if the original maximum intensity value of the image is higher than 255. Regardless of the pre-processing version, all the default pre-processing of nnU-Net were performed on the training data.

# 3 Results

We present the results of the LODO cross-validation per dataset, and per label with DSC and Hausdorff distance. The performance of the network was compared to the registration-based method described in the methods section 2.3. Additionally, we evaluated the performance of the network on several datasets from different centers in the testing on unseen datasets section. Next, we performed an ablation study to evaluate the cross-domain transportability of the network. Finally, we present another ablation study to evaluate the importance of the pre-processing steps.

## 3.1 LODO evaluation

The performance of each network on the left out dataset was compared to the gold standard (Figure 3). Each data point was calculated as the average DSC of a subject in the dataset. The number of subjects in each dataset are shown in Table 1. Networks showed similar performance on different datasets, with small variations seen as better performance on ADNI, PPMI, OASIS3, ABIDE-II, and MIRIAD, and a slightly worse performance on the SRH, and HCP datasets. The average DSC of all cross-validation subjects was  $0.89 \pm 0.03$ , and the AHD across all cross-validation subjects was  $0.13 \pm 0.12$ .

Figure 4 shows the DSC and the AHD per structure across all cross-validation subjects. For this plot we examined the average DSC of the structure on the right and the left hemisphere, as they normally show a similar performance. Similarly, we examined the average value for the AHD plot. Better performance on large structures such as CA and THAL is observed compared to small structures, such as HN, VPL, and VIM.

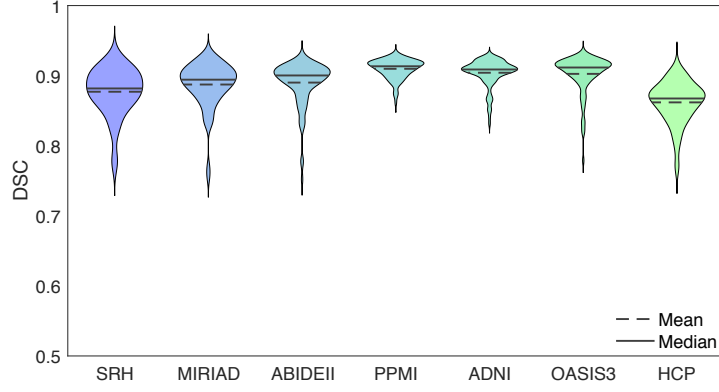


Figure 3: **LODO cross-validation performance.** The performance of each fold was measured with DSC on the left out dataset. The average DSC of each subject was calculated for all labels excluding the brain mask. Subjects belonging to the same fold were plotted together. The average DSC of the folds were  $0.88 \pm 0.03$ ,  $0.89 \pm 0.03$ ,  $0.89 \pm 0.03$ ,  $0.91 \pm 0.01$ ,  $0.90 \pm 0.02$ ,  $0.90 \pm 0.03$ , and  $0.86 \pm 0.03$  on SRH, MIRIAD, ABIDE-II, PPMI, ADNI, OASIS3, and HCP datasets respectively.

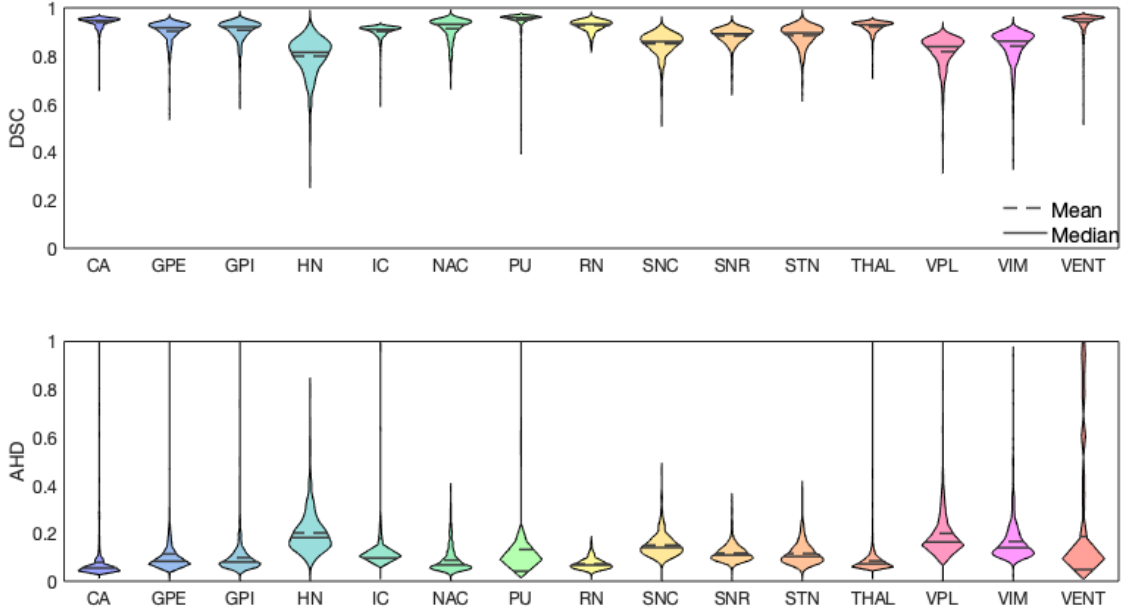


Figure 4: **LODO cross-validation performance on each label.** On the top, the DSC of each label was measured for all the training subjects during LODO cross-validation. For each subject, the DSC value was measured separately for the left and the right hemisphere, then averaged for the plot. Similarly, on the bottom, the AHD is measured. The full name of the labels can be find in table S3.

### 3.2 Testing on unseen datasets

The performance of the network was evaluated on 7 unseen datasets from different centers. The average DSC over all test subjects was  $0.89 \pm 0.04$ , and the AHD was  $0.12 \pm 0.07$ . Figure 5 shows the performance of the network on each dataset separately. Each data point in the violin plot is the average DSC of a subject in the dataset. There is less DSC between the network's output and the gold standard in the CHL and some of the CUB data, compared to the other datasets.

In Figure S10, the average DSC and AHD of all test data is shown per structure. Similar performance to the LODO cross-validation results is reported.

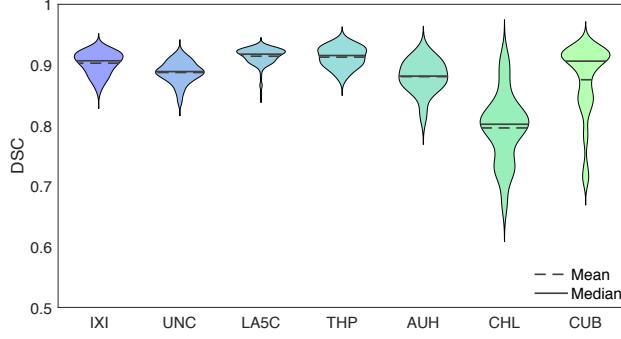


Figure 5: **The network’s performance on the unseen datasets (Test sets).** The average DSC of each subject was calculated for all its labels excluding the brain mask. The subjects belonging to the same dataset were plotted together. The average DSC of the datasets were  $0.90 \pm 0.02$ ,  $0.89 \pm 0.02$ ,  $0.91 \pm 0.01$ ,  $0.91 \pm 0.02$ ,  $0.88 \pm 0.03$ ,  $0.80 \pm 0.06$ , and  $0.88 \pm 0.06$  for IXI, UNC, LA5C, THP, AUH, CHL, and CUB respectively.

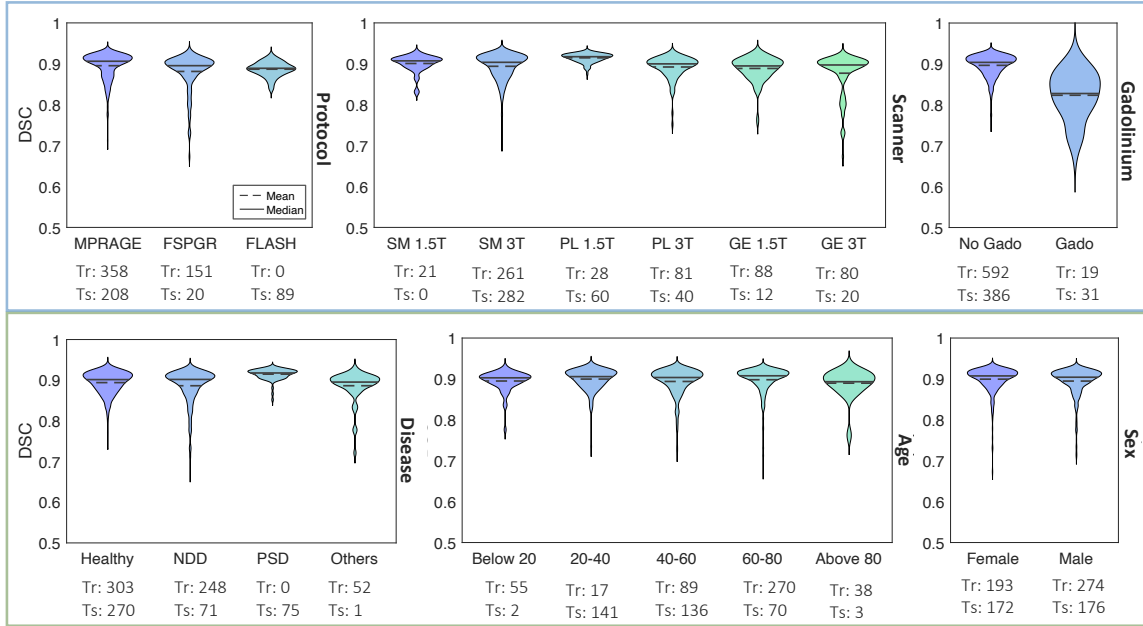


Figure 6: **Analysis of DSC stratified by potential confounding factors.** The factors were obtained from the causal diagram (Figure 2). **Top row (blue background):** factors affecting the acquisition conditions. **Bottom row (green background):** factors affecting the patient’s characteristics. The size of each class in the training set (Tr), and the Test set (Ts) are shown on the bottom of the plots. For the disease plot we classified the patient’s state of health into 4 classes of Healthy; Neurodegenerative disorders (NDD): AD, DM, MC, CI, OD, ESP, ET, and DT; Psychiatric disorders (PSD): BP, SCHZ, ADHD; and Others: AT, EP, PN. For the full name of the diseases please refer to table 1.

### 3.3 Ablation study on cross-domain transportability

We examine the influence of different factors (from the causal diagram) on the DSC between the network and the gold standard. All cross-validation and test data were divided into different classes of each factor. For the acquisition conditions, we divided the data according to acquisition protocol (3 classes: MPRAGE, FSPGR, FLASH), scanner (6 classes: Siemens 1.5/3T, Philips 1.5/3T, GE 1.5/3T), and the use of gadolinium (2 classes: used or not)(Figure 6- blue background). For the subjects characteristics, we divided the data according to the disease (4 classes: healthy, NeuroDegenerative Disorders-NDD, and PSYchiatric Disorders-PSD, and others), age (5 classes: below 20, 20-40, 40-60, 60-80, and above 80 years), and sex (2 classes: female, and male)(Figure 6- green background). For all factors,

including protocol, scanner, disease, age, and sex, the network demonstrated similar performance on different classes, indicating its generalizability across different domains, except in the gadolinium plot (Figure 6).

At the bottom of the plot 6, the number of subjects from each class in the training data (Tr), and the test data (Ts) are shown. The number of subjects with the FLASH protocol during the training was zero, while there were 89 FLASH data in the test set. The network showed a good performance on the unseen protocol, indicating its domain adaptation. Similarly, no scan from subjects with psychiatric disorders was used during the training, while the network performed well on subjects with psychiatric disorders (e.g. LA5C dataset).

Furthermore, we evaluated the performance of the network on 53 scans from a dataset with 7 Tesla T1w data (ATAG-7T,<sup>16</sup>) [66]. The network output a reasonable segmentation (evaluated by an expert), while the registration-based method failed. This shows the network’s domain adaptation on the new ultra-highfield imaging data, and the robustness of the method (Figure S14).

Another example of the method’s robustness can be seen in cases where the scan consists of a half brain. In these cases, the network output reasonable segmentations (evaluated by an expert), while the registration-based method failed (Figure S15).

### 3.4 Gadolinium

In Figure 6, the plot stratified by gadolinium revealed a clear difference between gadolinium vs. non-gadolinium. To ensure that the visible difference between the two classes is caused by the use of gadolinium and not by a confounder (e.g. scanner, protocol differences), we split the gadolinium and non-gadolinium data separately for each dataset. Among the test data, two datasets with gadolinium images were available (CHL and CUB). We observed lower DSC in the test data with gadolinium enhancement compared to non-gadolinium data in both CHL and CUB dataset (Figure S11).

To further study the effect of the gadolinium, we used two scans from the same patient, one with gadolinium and one without. When we used the non-gadolinium data both as the network input and to generate the registration-based gold standard, we got a DSC of 0.87. However, when we used the gadolinium data for both the network and the gold standard, we got the DSC of 0.73 (Figure 7). To evaluate whether the reduction in the DSC was caused by the network or by the gold standard, we compared the robustness of both methods. For this, we measured the DSC between the network’s output on the gadolinium and non-gadolinium scan, resulted in a DSC of 0.83. Similarly, the DSC between the gold standard method on the gadolinium and non-gadolinium scan was measured, resulted in a DSC of 0.77. This shows that the network is more robust in response to gadolinium compared to the gold standard registration-based method.

Next, we compared the DSC between the networks output on the gadolinium scan with the gold standard generated using the non-gadolinium scan, resulting in a DSC of 0.79. This confirms that the low 0.73 DSC is not only because of the network’s performance. As the non-gadolinium scans are not available for the CHL and the CUB data, we decided to heuristically reduce the high intensity of the vessels and generate gadolinium\* scans, which is a primary effect of the gadolinium on the contrast of the scan. When we used the gadolinium\* data instead of the original gadolinium data, the average DSC increased from  $0.78 \pm 0.05$  to  $0.84 \pm 0.04$  in the CHL data and from  $0.81 \pm 0.06$  to  $0.85 \pm 0.03$  in the CUB data (Figure 8).

### 3.5 Ablation study on the pre-processing

We evaluated the importance of different pre-processing steps used in this study. The average DSC across all cross-validation data are compared between 5 networks, one with no pre-processing, and four networks with pre-processing version 1 to 4 (V1: LPI, V2: LPI, 1mm voxel, V3: LPI, 1mm voxel, 256 dimension, V4: LPI, 1mm voxel, 256 dimension, 0-255 intensity; see method section for further information on the different versions 2.8).

There is a considerable difference between the network with no pre-processing and the network with the V1 pre-processing. In figure S13, we can see that the nnU-Net alone fails to generalize on the MIRIAD dataset, which shows the importance of conforming all the MR images to the same orientation. The network with the V3 pre-processing shows the best performance compared to V1 and V2. It has a higher average DSC compared to V1 and lower variation compared to both V1 and V2. The difference between the V3 and V4 networks is negligible, meaning that normalizing the images between the intensity range of 0-255 is not necessary. We conclude that conforming the MR images to the same orientation, voxel spacing and the dimension (pre-processing V3), prior to the nnU-Net default pre-processing, improves the performance of the network and the main improvement is obtained by the reorientation.

<sup>16</sup>[https://www.nitrc.org/projects/atag\\_mri\\_scans/](https://www.nitrc.org/projects/atag_mri_scans/)

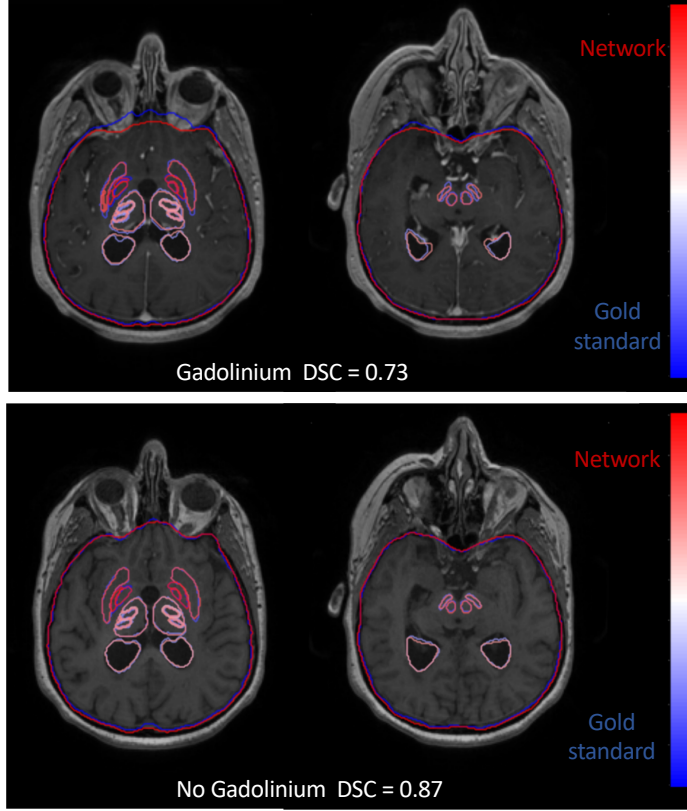


Figure 7: **The segmentation output of the network and the gold standard on the gadolinium and non-gadolinium scan of the same subject.** The network segmentations are shown in a gradient of red, and the gold standard segmentations are shown in a gradient of blue. Two axial slices of the same scan are shown in this figure, on top for the gadolinium enhanced scan, and on the bottom for the scan without the gadolinium enhancement. The DSC between the network and the gold standard is written below the image.

### 3.6 Brain mask

In addition to the deep brain structures, the network outputs a brain mask. The brain mask was compared with the brain mask obtained by the `antsBrainExtraction` function of ANTs (Figure S12). The average DSC between the two brain masks was  $0.97 \pm 0.01$  among all the cross-validation data and  $0.98 \pm 0.08$  among all the test data.

### 3.7 Time efficiency

The inference time of the network depends on the number of networks (folds) used for the ensemble. We provide 7 different folds. Figure S16 shows the comparison between the performance of the network on 50 test images using different number of folds for the ensembling, as well as the time required for the inference respectively. We suggest an ensemble of two folds as a reasonable trade-off between performance and low inference time.

Another factor affecting the inference time, is the computational power. Our method leverages the available GPU, while ANTs uses all available CPUs, therefore, to have a fair comparison, in table 2, we compared the inference time of DBSegment and ANTs using different computational power. In the presence of a GPU, our method is  $\sim 40$  times faster than ANTs, and in the absence of a GPU, it is  $\sim 13$  times faster. For instance, with 8 CPU and 1 GPU performed on a node of a high performance computing cluster, the average time required for our network’s inference was  $\sim 1.3$  minute to output both the segmentation and the brain mask in the patient’s space, while the registration-based method (using ANTs) on average required  $\sim 43$  minutes for the segmentation. Additionally, the average time required for obtaining the brain mask with ANTs was  $\sim 53$  minutes. There are faster ways to obtain a less accurate brain masks (e.g. *bet* function of FSL), therefore, we didn’t consider the time ANTs required to obtain a brain mask in table 2.

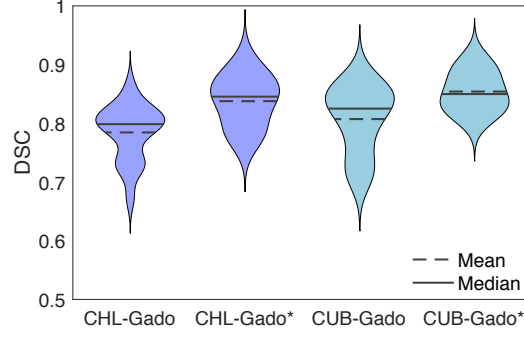


Figure 8: **Comparison of the DSC between the original gadolinium enhanced data and the gadolinium\* data.** The gadolinium\* are the data, where the high intensity of the vessels is reduced to imitate the morphology of the scans without the gadolinium enhancement. The comparison was done separately for the gadolinium data of the CHL and CUB datasets.

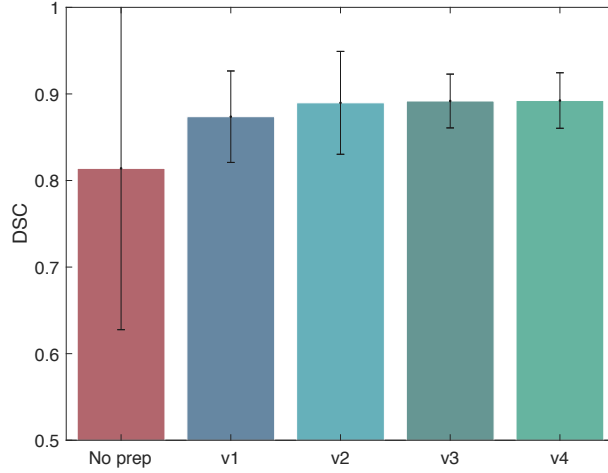


Figure 9: **Results of the ablation study on the pre-processing steps.** The DSC performance of five networks with different pre-processing steps are presented for all cross-validation data. Standard deviations across subjects are presented on top of the bar plots. The first network is not using any pre-processing. The second network, builds on the V1 pre-processing, conforming all MR images to the same orientation. For the V2 pre-processing, all MR images were conformed to the same orientation and  $1 \times 1 \times 1$  mm voxel spacing, in V3, MR images were conformed to the same orientation,  $1 \times 1 \times 1$  mm voxel spacing and  $256 \times 256 \times 256$  dimension, in V4, MR images were conformed to the same orientation,  $1 \times 1 \times 1$  mm voxel spacing,  $256 \times 256 \times 256$  dimension, and the intensity range of each image was normalized between 0-255.

## 4 Discussion

We presented a deep learning-based network segmenting 30 deep brain structures and a brain mask. We evaluated the performance of the network on diverse datasets in multiple steps, using a LODO cross-validation, testing on unseen datasets, and different ablation studies. The network segments quickly with high accuracy and robustness.

### 4.1 Networks evaluation

In the results of the LODO cross-validation (Figure 3), we observed a lower average DSC in the SRH and the HCP dataset. We suggest that the lower DSC in the SRH dataset is associated with the 19 subjects with the gadolinium scans. For the HCP dataset, we believe that the high quality of the data separates it from the other datasets. Our network, which is trained on 6 datasets with of a typical quality, is then evaluated on a high-quality dataset, resulting in lower DSC. Given that the HCP dataset is used as a training data in the 6 other folds, we think that the final network can generalize to high quality data.



Computational power	DBSegment	ANTs
1 GPU, 2 CPU	2.6	149
1 GPU, 4 CPU	1.9	79
1 GPU, 6 CPU	1.4	56
1 GPU, 8 CPU	1.3	43
1 GPU, 16 CPU	1.1	30
0 GPU, 2 CPU	10.2	133
0 GPU, 4 CPU	5	74
0 GPU, 6 CPU	4.2	52
0 GPU, 8 CPU	2.6	42
0 GPU, 16 CPU	2.4	32

Table 2: **Comparison of the time required for the inference of DBSegment and ANTs using different computational power.** The values are reported in minutes.

Examining the DSC plot for the structures, there was a better performance on large structures compared to small ones. This is expected, as DSC measures the volume similarly, and a slight difference in a small volume can lead to a considerable reduction in the DSC. We further evaluated the final ensemble network on 7 additional unseen datasets. A lower average DSC was observed in the CHL dataset and similarly in some of the CUB datasets, which we suggest is caused by the gadolinium enhancement.

A direct comparison of our method and other methods is not feasible, as the gold standard and the test data are different. However, in a superficial comparison our deep learning-based method has a better or a comparable performance to the existing methods, when comparing the commonly segmented deep brain structures [50, 2, 48, 67, 51, 68, 49, 44].

## 4.2 High diversity in clinical data

We used a diverse dataset for training as well as testing. This dataset contained data from 10 publicly available research oriented datasets, together with data from 4 clinical centers. Higher variation was observed in the clinical data (AUH, CUB, CHL, and RSH) compared to the research oriented ones (Figure 3, and 5). Data from research-oriented datasets appears to be more standardized than clinical data due to strict protocols and homogeneity of procedures. In clinical practice, however, patient, clinician and center variability is to be expected. For example, we qualitatively observed much more patient head tilt in clinical acquisitions. Therefore, the clinical data is expected to be more variable and harder to generalize an automated method from. In most previous studies, access to clinical data was limited. We note this as a strength of this study, because we used a clinical dataset for the training and three in the test set. This provides evidence that our method can be adapted for clinical practice.

## 4.3 Ablation study on cross-domain transportability

As presented in our causal diagram (Figure 2), there are various factors affecting the final DSC. We separated the data to different classes of each factor to see if performance was particularly low in one class. However, to isolate effects of each factor, other factors should ideally remain constant. For instance, age and the disease are in a chain that makes them dependent to each other, so when we look at the age plot, and we observe slightly lower performance in the class "above 80", this could be associated with the higher prevalence of diseases in older ages, especially neurodegenerative disorders, rather than age solely.

We also considered the existence of the confounders. For instance, the outliers in the GE 3T scanner and the FSPGR protocol are probably caused by the effect of gadolinium in the CHL data (the CHL data are acquired with GE 3T and FSPGR protocol, Table 1), rather than the type of scanner or the acquisition protocol. Therefore, in cases of clear differences between the classes, such as gadolinium and non-gadolinium, we controlled the corresponding meta data further.

## 4.4 Gadolinium enhancement

Using clinical data, we observed that the use of gadolinium is very common in clinical practice, but we could not find any publicly available research oriented dataset using gadolinium enhancement. Our analysis indicates that our approach is more robust (0.83 DSC between the gadolinium and non-gadolinium scan) to the presence of gadolinium compared to the registration-based method (0.77 DSC between the gadolinium and non-gadolinium scan). Presented in Figure 7, there is a clear difference between the registration-based segmentation of SN and brain mask in the gadolinium

and the non-gadolinium scan, while the difference in our network’s segmentation is small. However, the segmentation of the right PU is changed between the gadolinium and non-gadolinium scan, for both the registration-based method and the network. In a registration-based segmentation, the patient’s MRI is mapped to a template. Most of the established templates are generated using non-gadolinium data. Therefore, there is a considerable difference in the appearance of the patient’s gadolinium-enhanced scan compared to the template, which can lead to an inaccurate registration.

#### 4.5 Ablation study on the pre-processing

We observed a low DSC on the MIRIAD dataset compared to the other datasets, when we trained a network with no prior pre-processing and just the default pre-processings of the nnU-Net (Figure S13). One of the main differences observed between the MIRIAD dataset compared to the other datasets was the orientation. Most of the data are orientated in this order: right/left, posterior/anterior, superior/inferior, while the data from the MIRIAD dataset have the last two axis swapped. Adapting the pre-processing strategy improved the performance on the MIRIAD dataset (Figure S13) [44]. This highlights the importance of the MR orientation in the method’s generalization.

#### 4.6 Limitations

We relied on the registration-based method to annotate the training data. Additionally, we evaluated the annotations of the registration-based method before training. Therefore, our training annotations are gold standard and not the ground truth. To have a ground truth, manual segmentations by more than one expert are required. If only one expert annotates the data, it might be prone to bias. However, manual segmentation of such a large dataset for 30 different structures is a very time consuming task.

While we improved the network’s performance on the gadolinium-enhanced data by imitating the non-gadolinium data, the average performance was lower than the other non-gadolinium data. In future work, we plan to apply domain adaptation techniques to improve the generalizability of the method to gadolinium-enhanced data.

We use T1w MRI for the whole procedure and did not consider additional sequences to this version of DBSegment for two reasons. Not all our datasets have a T2 sequence, and as we want to have a diverse dataset for training and testing, we decided to keep all the datasets, instead of using only the ones that have both T1 and T2. Furthermore, we didn’t want to have the constraint of having both T1 and T2 for the users, so that with having only a T1, the segmentation would be possible. However, we are planning to develop a multi-spectral version of DBSegment, where the network can leverage information from different MRI sequences or even different imaging modalities.

### 5 Conclusion

In this paper we presented a method to segment 30 deep brain structures and a brain mask from T1w MRI scans. The method performed almost as well as the registration-based method ( $DSC = 0.89 \pm 0.04$ ), while reducing the required time significantly, and enhancing the robustness. Furthermore, we assessed the cross-domain transportability by evaluating the performance of the network separately on different domains of the factors affecting the performance. Finally, we provide the method as an easy-to-use python package.

#### 5.1 Code availability

The source code of the method is available under GPL licence on <https://github.com/luxneuroimage/DBSegment>. An easy-to-use python package is available via *pip* (`pip install DBSegment`, see <https://pypi.org/project/DBSegment/>). In the toolbox, we also provided an additional network, where instead of segmenting Subthalamic Nucleus (STN) as a whole, the sub-parts of STN, Sensorimotor, Limbic, and Associative are segmented. The trained model files are provided via [https://webdav-r3lab.uni.lu/public/deep\\_brain\\_seg/deep\\_brain\\_seg\\_model\\_7f.zip](https://webdav-r3lab.uni.lu/public/deep_brain_seg/deep_brain_seg_model_7f.zip).

### 6 Acknowledgments

M.B.’s work was funded by the Fonds National de la Recherche (FNR), Luxembourg, grant AFR ref. 12548237. M.V.P.’s work was supported by Jascha Fonden and the Lundbeck Foundation. J.G. was partly supported by the 111 Project on Computational Intelligence and Intelligent Control, ref B18024. A.Ho. was supported by the German Research Foundation (Deutsche Forschungsgemeinschaft, Emmy Noether Stipend 410169619 and 424778381 – TRR 295). A.Ho. is participant in the BIH-Charité Clinician Scientist Program funded by the Charité –Universitätsmedizin Berlin and the Berlin Institute of Health. The collaboration of J.G, A.Ho., F.H. and A.Hu. was fostered by the EU Joint

Programme - Neurodegenerative Disease Research (JPND) project *DynaStim*. The project is supported through the following funding organisations under the aegis of JPND - [www.jpnd.eu](http://www.jpnd.eu): German Federal Ministry of Education and Research (BMBF), Luxembourg National Research Fund (FNR), The Netherlands Organisation for Health Research and Dev. (ZonMw), Swedish Research Council (SRC). A. Hu.'s work was partly supported by the Fondation Cancer Luxembourg.

We thank Dr. Chencheng Zhang, Shanghai Ruijin Hospital, Shanghai, China, for providing anonymized clinical data for this study.

We thank Dr. Clemens Neudorfer, Charité Universitätsmedizin Berlin, for assisting with providing anonymized clinical study data.

We also thank Beatriz Garcia Santa Cruz, M.Sc., Centre Hospitalier de Luxembourg, for her comments on the causal diagram. The experiments presented in this paper were carried out using the HPC facilities of the University of Luxembourg [69].

Data used in the preparation of this work were obtained from the Human Connectome Project (HCP) database (<https://ida.loni.usc.edu/login.jsp>). The HCP project (Principal Investigators: Bruce Rosen, M.D., Ph.D., Martinos Center at Massachusetts General Hospital; Arthur W. Toga, Ph.D., University of Southern California, Van J. Weeden, MD, Martinos Center at Massachusetts General Hospital) is supported by the National Institute of Dental and Craniofacial Research (NIDCR), the National Institute of Mental Health (NIMH) and the National Institute of Neurological Disorders and Stroke (NINDS). HCP is the result of efforts of co-investigators from the University of Southern California, Martinos Center for Biomedical Imaging at Massachusetts General Hospital (MGH), Washington University, and the University of Minnesota.

Data used in the preparation of this article were obtained from the Parkinson's Progression Markers Initiative (PPMI) database ([www.ppmi-info.org/data](http://www.ppmi-info.org/data)). For up-to-date information on the study, visit [www.ppmi-info.org](http://www.ppmi-info.org)." PPMI – a public-private partnership – is funded by The Michael J. Fox Foundation for Parkinson's Research and funding partners, including, AbbVie, , AcureX Therapeutics , Allergan, Amathus Therapeutics, Aligning Science Across Parkinson's, Avid Radiopharmaceuticals, BIAL Biotech, Biogen, BioLegend, Bristol-Myers Squibb, Calico, Celgene, Dacapo, Denali, 4D Pharma plc, Edmond J. Safra philanthropic foundation, GE Healthcare, Genentech, GlaxoSmithKline, Golub Capital, Handl Therapeutics, Insitro, Janssen Neuroscience, Eli Lilly, Lundbeck, MERCK, Meso Scale Discovery, , Neurocrine Biosciences, Pfizer, Piramal Imaging, Prevail Therapeutics, Roche, Sanofi Genzyme, Servier, Takeda, Teva, UCB, Verily, Voyager Therapeutics.

Data were provided in part by OASIS-3: Principal Investigators: T. Benzinger, D. Marcus, J. Morris; NIH P50 AG00561, P30 NS09857781, P01 AG026276, P01 AG003991, R01 AG043434, UL1 TR000448, R01 EB009352. AV-45 doses were provided by Avid Radiopharmaceuticals, a wholly owned subsidiary of Eli Lilly.

Data used in the preparation of this article were obtained from the MIRIAD database. The MIRIAD investigators did not participate in analysis or writing of this report. The MIRIAD dataset is made available through the support of the UK Alzheimer's Society (Grant RF116). The original data collection was funded through an unrestricted educational grant from GlaxoSmithKline (Grant 6GKC).

The MR brain images from healthy volunteers of the UNC dataset used in this paper were collected and made available by the CASILab at The University of North Carolina at Chapel Hill and were distributed by the MIDAS Data Server at Kitware, Inc.

## Declaration of competing interest

The authors declare no competing interests.

## References

- [1] Rolf A. Heckemann, Shiva Keihaninejad, Paul Aljabar, Daniel Rueckert, Joseph V. Hajnal, and Alexander Hammers. Improving intersubject image registration using tissue-class information benefits robustness and accuracy of multi-atlas based anatomical segmentation. *NeuroImage*, 51(1):221–227, 2010.
- [2] Fausto Milletari, Seyed-Ahmad Ahmadi, Christine Kroll, Annika Plate, Verena Rozanski, Juliana Maiostre, Johannes Levin, Olaf Dietrich, Birgit Ertl-Wagner, Kai Bötzel, and Nassir Navab. Hough-CNN: Deep learning for segmentation of deep brain regions in MRI and ultrasound. *Computer Vision and Image Understanding*, 164:92–102, nov 2017.

- [3] D L Pham, C Xu, and J L Prince. Annu rev biomed eng. *Annu Rev Biomed Eng*, 2:315–337, 2000.
- [4] Gunther Helms, Bogdan Draganski, Richard Frackowiak, John Ashburner, and Nikolaus Weiskopf. Improved segmentation of deep brain grey matter structures using magnetization transfer (MT) parameter maps. *NeuroImage*, 47(1):194–198, 2009.
- [5] Yun Jung Bae, Jong Min Kim, Chul Ho Sohn, Ji Hyun Choi, Byung Se Choi, Yoo Sung Song, Yoonho Nam, Se Jin Cho, Beomseok Jeon, and Jae Hyoung Kim. Imaging the substantia nigra in Parkinson disease and other Parkinsonian syndromes. *Radiology*, 300(2):260–278, 2021.
- [6] Dibash Basukala, Ramakrishnan Mukundan, Anthony Lim, Michael A. Hurrell, Ross J. Keenan, John C. Dalrymple-Alford, Tim J. Anderson, Daniel J. Myall, and Tracy R. Melzer. Automated segmentation of substantia nigra and red nucleus using quantitative susceptibility mapping images: Application to Parkinson’s disease. *Computers and Electrical Engineering*, 91(December 2020), 2021.
- [7] Andreas Horn and Andrea A. Kühn. Lead-DBS: A toolbox for deep brain stimulation electrode localizations and visualizations. *NeuroImage*, 107:127–135, 2015.
- [8] Erik H. Middlebrooks, Vanessa M. Holanda, Ibrahim S. Tuna, Hrishikesh D. Deshpande, Markus Bredel, Leonardo Almeida, Harrison C. Walker, Barton L. Guthrie, Kelly D. Foote, and Michael S. Okun. A method for pre-operative single-subject thalamic segmentation based on probabilistic tractography for essential tremor deep brain stimulation. *Neuroradiology*, 60(3):303–309, 2018.
- [9] Peter C. Reinacher, Bálint Várkuti, Marie T. Krüger, Tobias Piroth, Karl Egger, Roland Roelz, and Volker A. Coenen. Automatic Segmentation of the Subthalamic Nucleus: A Viable Option to Support Planning and Visualization of Patient-Specific Targeting in Deep Brain Stimulation. *Operative Neurosurgery*, 17(5):497–502, 2019.
- [10] Alim Louis Benabid. Deep brain stimulation for Parkinson’s disease. *Current Opinion in Neurobiology*, 13(6):696–706, 2003.
- [11] Jan Herzog, Jens Volkmann, Paul Krack, Florian Kopper, Monika Pötter, Delia Lorenz, Meike Steinbach, Stefan Klebe, Wolfgang Hamel, Bettina Schrader, Dieter Weinert, Dieter Müller, Hubertus M. Mehdorn, and Günther Deuschl. Two-year follow-up of subthalamic deep brain stimulation in Parkinson’s disease. *Movement Disorders*, 18(11):1332–1337, 2003.
- [12] Paul S. Larson. Deep Brain Stimulation for Movement Disorders. *Neurotherapeutics*, 11(3):465–474, 2014.
- [13] James L. Abelson, George C. Curtis, Oren Sagher, Ronald C. Albucher, Mark Harrigan, Stephan F. Taylor, Brian Martis, and Bruno Giordani. Deep brain stimulation for refractory obsessive-compulsive disorder. *Biological Psychiatry*, 57(5):510–516, 2005.
- [14] Olga Dergachyova, Yulong Zhao, Claire Haegelen, Pierre Jannin, and Caroline Essert. Automatic preoperative planning of DBS electrode placement using anatomic-clinical atlases and volume of tissue activated. *International Journal of Computer Assisted Radiology and Surgery*, 13(7):1117–1128, 2018.
- [15] Brian T. Wang, Stefan Poirier, Ting Guo, Andrew G. Parrent, Terry M. Peters, and Ali R. Khan. Generation and evaluation of an ultra-high-field atlas with applications in DBS planning. *Medical Imaging 2016: Image Processing*, 9784:97840H, 2016.
- [16] Nicola Pavese, Yen F. Tai, Nada Yousif, Dipankar Nandi, and Peter G. Bain. Traditional Trial and Error versus Neuroanatomic 3-Dimensional Image Software-Assisted Deep Brain Stimulation Programming in Patients with Parkinson Disease. *World Neurosurgery*, 134:e98–e102, 2020.
- [17] Daria Nesterovich Anderson, Braxton Osting, Johannes Vorwerk, Alan D. Dorval, and Christopher R. Butson. Optimized programming algorithm for cylindrical and directional deep brain stimulation electrodes. *Journal of Neural Engineering*, 15(2), 2018.
- [18] Ruben Cubo, Markus Fahlström, Elena Jiltsova, Helena Andersson, and Alexander Medvedev. Calculating deep brain stimulation amplitudes and power consumption by constrained optimization. *Journal of Neural Engineering*, 16(1), 2019.
- [19] Mattias Åström, Jennifer Samuelsson, Jonas Roothans, Anders Fytagoridis, Maxim Ryzhkov, Rutger Nijluning, and Patric Blomstedt. Prediction of electrode contacts for clinically effective deep brain stimulation in essential tremor. *Stereotactic and Functional Neurosurgery*, 96(5):281–288, 2018.
- [20] Fedde Van Der Lijn, Marleen De Bruijne, Stefan Klein, Tom Den Heijer, Yoo Y. Hoogendam, Aad Van Der Lugt, Monique M.B. Breteler, and Wiro J. Niessen. Automated brain structure segmentation based on atlas registration and appearance models. *IEEE Transactions on Medical Imaging*, 31(2):276–286, 2012.

- [21] Sandra González-villà, Arnau Oliver, Sergi Valverde, Liping Wang, Reyer Zwiggelaar, and Xavier Lladó. Artificial Intelligence in Medicine A review on brain structures segmentation in magnetic resonance imaging. *Artificial Intelligence In Medicine*, 73:45–69, 2016.
- [22] VS Fonov, AC Evans, RC McKinstry, CR Alml, and DL Collins. Unbiased nonlinear average age-appropriate brain templates from birth to adulthood. *NeuroImage*, 47:S102, 2009.
- [23] Jonathan C. Lau, Keith W. MacDougall, Miguel F. Arango, Terry M. Peters, Andrew G. Parrent, and Ali R. Khan. Ultra-High Field Template-Assisted Target Selection for Deep Brain Stimulation Surgery. *World Neurosurgery*, 103:531–537, 2017.
- [24] Wolfgang M. Pauli, Amanda N. Nili, and J. Michael Tyszka. Data Descriptor: A high-resolution probabilistic in vivo atlas of human subcortical brain nuclei. *Scientific Data*, 5:1–13, 2018.
- [25] Jiahui Wang, Clement Vachet, Ashley Rumble, Sylvain Gouttard, Clémentine Ouziel, Emilie Perrot, Guangwei Du, Xuemei Huang, Guido Gerig, and Martin Styner. Multi-atlas segmentation of subcortical brain structures via the AutoSeg software pipeline. *Frontiers in Neuroinformatics*, 8(FEB):1–11, 2014.
- [26] Dorian Vogel, Ashesh Shah, Jérôme Coste, Jean Jacques Lemaire, Karin Wårdell, and Simone Hemm. Anatomical brain structures normalization for deep brain stimulation in movement disorders. *NeuroImage: Clinical*, 27(April):102271, 2020.
- [27] Siobhan Ewert, Philip Plettig, Ningfei Li, M. Mallar Chakravarty, D. Louis Collins, Todd M. Herrington, Andrea A. Kühn, and Andreas Horn. Toward defining deep brain stimulation targets in MNI space: A subcortical atlas based on multimodal MRI, histology and structural connectivity. *NeuroImage*, 170(January 2017):271–282, 2018.
- [28] Jason H. Su, Francis T. Thomas, Willard S. Kasoff, Thomas Tourdias, Eun Young Choi, Brian K. Rutt, and Manojkumar Saranathan. Thalamus Optimized Multi Atlas Segmentation (THOMAS): fast, fully automated segmentation of thalamic nuclei from structural MRI. *NeuroImage*, 194(February):272–282, 2019.
- [29] Brian B Avants, Nick Tustison, et al. Advanced normalization tools (ants). 2009.
- [30] Mark Jenkinson and Stephen Smith. A global optimisation method for robust affine registration of brain images. *Medical Image Analysis*, 5(2):143–156, 2001.
- [31] Mark Jenkinson, Peter Bannister, Michael Brady, and Stephen Smith. Improved Optimization for the Robust and Accurate Linear Registration and Motion Correction of Brain Images. *NeuroImage*, 17(2):825–841, 2002.
- [32] J L R Andersson, M Jenkinson, and S Smith. Non-linear registration, aka spatial normalization (FMRIB technical report TR07JA2). (June), 2010.
- [33] John Ashburner and Karl J. Friston. Unified segmentation. *NeuroImage*, 26(3):839–851, 2005.
- [34] John Ashburner. A fast diffeomorphic image registration algorithm. *NeuroImage*, 38(1):95–113, 2007.
- [35] John Ashburner and Karl J. Friston. Diffeomorphic registration using geodesic shooting and Gauss-Newton optimisation. *NeuroImage*, 55(3):954–967, 2011.
- [36] Yangming Ou, Aristeidis Sotiras, Nikos Paragios, and Christos Davatzikos. DRAMMS: Deformable registration via attribute matching and mutual-saliency weighting. *Medical Image Analysis*, 15(4):622–639, 2011.
- [37] Xiang Feng, Andreas Deistung, Michael G. Dwyer, Jesper Hagemeier, Paul Polak, Jessica Lebenberg, Frédérique Frouin, Robert Zivadinov, Jürgen R. Reichenbach, and Ferdinand Schweser. An improved FSL-FIRST pipeline for subcortical gray matter segmentation to study abnormal brain anatomy using quantitative susceptibility mapping (QSM). *Magnetic Resonance Imaging*, 39:110–122, 2017.
- [38] Thomas Schönecker, A. Kupsch, A. A. Kühn, G. H. Schneider, and K. T. Hoffmann. Automated optimization of subcortical cerebral MR imaging-atlas coregistration for improved postoperative electrode localization in deep brain stimulation. *American Journal of Neuroradiology*, 30(10):1914–1921, 2009.
- [39] Andreas Husch, Mikkel V. Petersen, Peter Gemmar, Jorge Goncalves, Niels Sunde, and Frank Hertel. Post-operative deep brain stimulation assessment: Automatic data integration and report generation. *Brain Stimulation*, 11(4):863–866, 2018.
- [40] Andreas Horn, Ningfei Li, Till A Dembeck, Ari Kappel, Chadwick Boulay, Siobhan Ewert, Anna Tietze, Andreas Husch, Thushara Perera, Wolf-Julian Neumann, Marco Reisert, Hang Si, Robert Oostenveld, Christopher Rorden, Fang-Cheng Yeh, Qianqian Fang, Todd M Herrington, Johannes Vorwerk, and Andrea A Kühn. Title Lead-DBS v2: Towards a comprehensive pipeline for deep brain stimulation imaging. *NeuroImage*, 184(3):293–316, 2019.
- [41] Hans Johnson, Greg Harris, and Kent Williams. BRAINSFit: mutual information rigid registrations of whole-brain 3D images, using the insight toolkit. *Insight J*, 57(1), 2007.

- [42] Douglas N. Greve and Bruce Fischl. Accurate and robust brain image alignment using boundary-based registration. *NeuroImage*, 48(1):63–72, 2009.
- [43] Mariano Cabezas, Arnau Oliver, Xavier Lladó, and Jordi Freixenet. A review of atlas-based segmentation for magnetic resonance brain images. *Computer Methods and Programs in Biomedicine*, 104(3):e158–e177, 2011.
- [44] Leonie Henschel, Sailesh Conjeti, Santiago Estrada, Kersten Diers, Bruce Fischl, and Martin Reuter. FastSurfer - A fast and accurate deep learning based neuroimaging pipeline. *NeuroImage*, 219:117012, 2020.
- [45] Zeynettin Akkus, Alfia Galimzianova, Assaf Hoogi, Daniel L Rubin, and Bradley J Erickson. Deep Learning for Brain MRI Segmentation : State of the Art and Future Directions. pages 449–459, 2017.
- [46] Alexandre De Br. Deep Neural Networks for Anatomical Brain Segmentation. pages 20–28, 2015.
- [47] Siqi Bao, Albert C S Chung, Siqi Bao, and Albert C S Chung. Computer Methods in Biomechanics and Biomedical Engineering : Imaging & Visualization Multi-scale structured CNN with label consistency for brain MR image segmentation Multi-scale structured CNN with label consistency for brain MR image segmentation. 1163(June), 2016.
- [48] Kaisar Kushibar, Sergi Valverde, Sandra González-villà, Jose Bernal, Mariano Cabezas, Arnau Oliver, and Xavier Lladó. Automated sub-cortical brain structure segmentation combining spatial and deep convolutional features. *Medical Image Analysis*, 48:177–186, 2018.
- [49] Abhijit Guha Roy, Sailesh Conjeti, Nassir Navab, and Christian Wachinger. QuickNAT: A Fully Convolutional Network for Quick and Accurate Segmentation of Neuroanatomy. 2018.
- [50] Raghav Mehta and Jayanthi Sivaswamy. M-NET : A CONVOLUTIONAL NEURAL NETWORK FOR DEEP BRAIN STRUCTURE SEGMENTATION Raghav Mehta , Jayanthi Sivaswamy Center for Visual Information Technology ( CVIT ), IIIT-Hyderabad , India. pages 437–440, 2017.
- [51] Essam A Rashed, Jose Gomez-tames, and Akimasa Hirata. End-to-end semantic segmentation of personalized deep brain structures for non-invasive brain stimulation. *Neural Networks*, 125:233–244, 2020.
- [52] Fabian Isensee, Paul F. Jaeger, Simon A.A. Kohl, Jens Petersen, and Klaus H. Maier-Hein. nnU-Net: a self-configuring method for deep learning-based biomedical image segmentation. *Nature Methods*, 18(2):203–211, 2021.
- [53] D. C. Van Essen, K. Ugurbil, E. Auerbach, D. Barch, T. E.J. Behrens, R. Bucholz, A. Chang, L. Chen, M. Corbetta, S. W. Curtiss, S. Della Penna, D. Feinberg, M. F. Glasser, N. Harel, A. C. Heath, L. Larson-Prior, D. Marcus, G. Michalareas, S. Moeller, R. Oostenveld, S. E. Petersen, F. Prior, B. L. Schlaggar, S. M. Smith, A. Z. Snyder, J. Xu, and E. Yacoub. The Human Connectome Project: A data acquisition perspective. *NeuroImage*, 62(4):2222–2231, 2012.
- [54] Adriana Di Martino, David O’Connor, Bosi Chen, Kaat Alaerts, Jeffrey S. Anderson, Michal Assaf, Joshua H. Balsters, Leslie Baxter, Anita Beggato, Sylvie Bernaerts, Laura M.E. Blanken, Susan Y. Bookheimer, B. Blair Braden, Lisa Byrge, F. Xavier Castellanos, Mirella Dapretto, Richard Delorme, Damien A. Fair, Inna Fishman, Jacqueline Fitzgerald, Louise Gallagher, R. Joanne Jao Keehn, Daniel P. Kennedy, Janet E. Lainhart, Beatriz Luna, Stewart H. Mostofsky, Ralph Axel Müller, Mary Beth Nebel, Joel T. Nigg, Kirsten O’Hearn, Marjorie Solomon, Roberto Toro, Chandan J. Vaidya, Nicole Wenderoth, Tonya White, R. Cameron Craddock, Catherine Lord, Bennett Leventhal, and Michael P. Milham. Enhancing studies of the connectome in autism using the autism brain imaging data exchange II. *Scientific Data*, 4:1–15, 2017.
- [55] Darko Aleksovski, Dragana Miljkovic, Daniele Bravi, and Angelo Antonini. Disease progression in Parkinson subtypes: the PPMI dataset. *Neurological Sciences*, 39(11):1971–1976, 2018.
- [56] Susanne G. Mueller, Michael W. Weiner, Leon J. Thal, Ronald C. Petersen, Clifford R. Jack, William Jagust, John Q. Trojanowski, Arthur W. Toga, and Laurel Beckett. Ways toward an early diagnosis in Alzheimer’s disease: The Alzheimer’s Disease Neuroimaging Initiative (ADNI). *Alzheimer’s and Dementia*, 1(1):55–66, 2005.
- [57] Pamela J LaMontagne, Tammie L S Benzinger, John C Morris, Sarah Keefe, Russ Hornbeck, Chengjie Xiong, Elizabeth Grant, Jason Hassenstab, Krista Moulder, Andrei G Vlassenko, Marcus E Raichle, Carlos Cruchaga, and Daniel Marcus. OASIS-3: Longitudinal Neuroimaging, Clinical, and Cognitive Dataset for Normal Aging and Alzheimer Disease. *medRxiv*, page 2019.12.13.19014902, jan 2019.
- [58] Ian B. Malone, David Cash, Gerard R. Ridgway, David G. MacManus, Sebastien Ourselin, Nick C. Fox, and Jonathan M. Schott. MIRIAD-Public release of a multiple time point Alzheimer’s MR imaging dataset. *NeuroImage*, 70:33–36, 2013.
- [59] R. A. Poldrack, E. Congdon, W. Triplett, K. J. Gorgolewski, K. H. Karlsgodt, J. A. Mumford, F. W. Sabb, N. B. Freimer, E. D. London, T. D. Cannon, and R. M. Bilder. A phenome-wide examination of neural and cognitive function. *Scientific Data*, 3:1–12, 2016.

- [60] Elizabeth Bullitt, Donglin Zeng, Guido Gerig, Stephen Aylward, Sarang Joshi, J. Keith Smith, Weili Lin, and Matthew G. Ewend. Vessel tortuosity and brain tumor malignancy: A blinded study. *Academic Radiology*, 12(10):1232–1240, 2005.
- [61] Vincent A. Magnotta, Joy T. Matsui, Dawei Liu, Hans J. Johnson, Jeffrey D. Long, Bradley D. Bolster, Bryon A. Mueller, Kelvin Lim, Susumu Mori, Karl G. Helmer, Jessica A. Turner, Sarah Reading, Mark J. Lowe, Elizabeth Aylward, Laura A. Flashman, Greg Bonett, and Jane S. Paulsen. MultiCenter Reliability of Diffusion Tensor Imaging. *Brain Connectivity*, 2(6):345–355, 2012.
- [62] Paul A. Yushkevich, Joseph Piven, Heather Cody Hazlett, Rachel Gimpel Smith, Sean Ho, James C. Gee, and Guido Gerig. User-guided 3D active contour segmentation of anatomical structures: Significantly improved efficiency and reliability. *NeuroImage*, 31(3):1116–1128, 2006.
- [63] Orhun Utku Aydin, Abdel Aziz Taha, Adam Hilbert, Ahmed A. Khalil, Ivana Galinovic, Jochen B. Fiebach, Dietmar Frey, and Vince Istvan Madai. On the usage of average Hausdorff distance for segmentation performance assessment: hidden error when used for ranking. *European Radiology Experimental*, 5(1), 2021.
- [64] Daniel C. Castro, Ian Walker, and Ben Glocker. Causality matters in medical imaging. *Nature Communications*, 11(1), 2020.
- [65] Michael A Ibrahim and AB Dublin. Magnetic resonance imaging (mri) gadolinium. *U: StatPearls [Internet]. Treasure Island (FL): StatPearls Publishing*, 2018.
- [66] Max C. Keuken, Pierre Louis Bazin, Andreas Schäfer, Jane Neumann, Robert Turner, and Birte U. Forstmann. Ultra-high 7T MRI of structural age-related changes of the subthalamic nucleus. *Journal of Neuroscience*, 33(11):4896–4900, 2013.
- [67] Mahsa Shakeri, Stavros Tsogkas, Enzo Ferrante, Sarah Lippe, Samuel Kadoury, Nikos Paragios, Iasonas Kokkinos, Universite Paris-saclay, and Polytechnique Montreal. SUB-CORTICAL BRAIN STRUCTURE SEGMENTATION USING F-CNN ' S University of Montreal , 4 Sainte-Justine Hospital Research Center. *Isbi 2016*, pages 269–272, 2016.
- [68] John S. H. Baxter, Ehouarn Maguet, and Pierre Jannin. Segmentation of the subthalamic nucleus in MRI via Convolutional Neural Networks for deep brain stimulation planning. (February):53, 2021.
- [69] S. Varrette, P. Bouvry, H. Cartiaux, and F. Georgatos. Management of an academic hpc cluster: The ul experience. In *Proc. of the 2014 Intl. Conf. on High Performance Computing & Simulation (HPCS 2014)*, pages 959–967, Bologna, Italy, July 2014. IEEE.

## Supplementary Material

Full name	Abbreviation	Source	Label
Brain Mask	BM	ANTs	1
Caudate Nucleus - Left	CA-L	CIT	2
Caudate Nucleus - Right	CA-R	CIT	3
Globus Pallidus Externus - Left	GPE-L	Distal	4
Globus Pallidus Externus - Right	GPE-R	Distal	5
Globus Pallidus Internus - Left	GPI-L	Distal	6
Globus Pallidus Internus - Right	GPI-R	Distal	7
Habenular Nuclei - Left	HN-L	Thomas	8
Habenular Nuclei - Right	HN-R	Thomas	9
Internal capsule - Left	IC-L	Distal	10
Internal capsule - Right	IC-R	Distal	11
Nucleus Accumbens - Left	NAC-L	CIT	12
Nucleus Accumbens - Right	NAC-R	CIT	13
Putamen - Left	PU-L	CIT	14
Putamen - Right	PU-R	CIT	15
Red nucleus - Left	RN-L	Distal	16
Red nucleus - Right	RN-R	Distal	17
Substantia Nigra, pars compacta - Left	SNC-L	CIT	18
Substantia Nigra, pars compacta - Right	SNC-R	CIT	19
Substantia Nigra, pars reticulata - Left	SNR-L	CIT	20
Substantia Nigra, pars reticulata - Right	SNR-R	CIT	21
Subthalamic Nucleus - Left	STN-L	Distal	22
Subthalamic Nucleus - Right	STN-R	Distal	23
Thalamus - Left	THAL-L	Thomas	24
Thalamus - Right	THAL-R	Thomas	25
Ventral lateral posterior nucleus of Thalamus - Right	VPL-R	Thomas	26
Ventral lateral posterior nucleus of Thalamus - Left	VPL-L	Thomas	27
Lateral ventricle - Left	VENT-L	Manual	28
Lateral ventricle - Right	VENT-R	Manual	29
Ventrolateral intermediate nucleus of Thalamus - Left	VIM-L	Thomas	30
Ventrolateral intermediate nucleus of Thalamus - Right	VIM-R	Thomas	31

Table S3: **The full name of the structures.** Label 0 is the background.



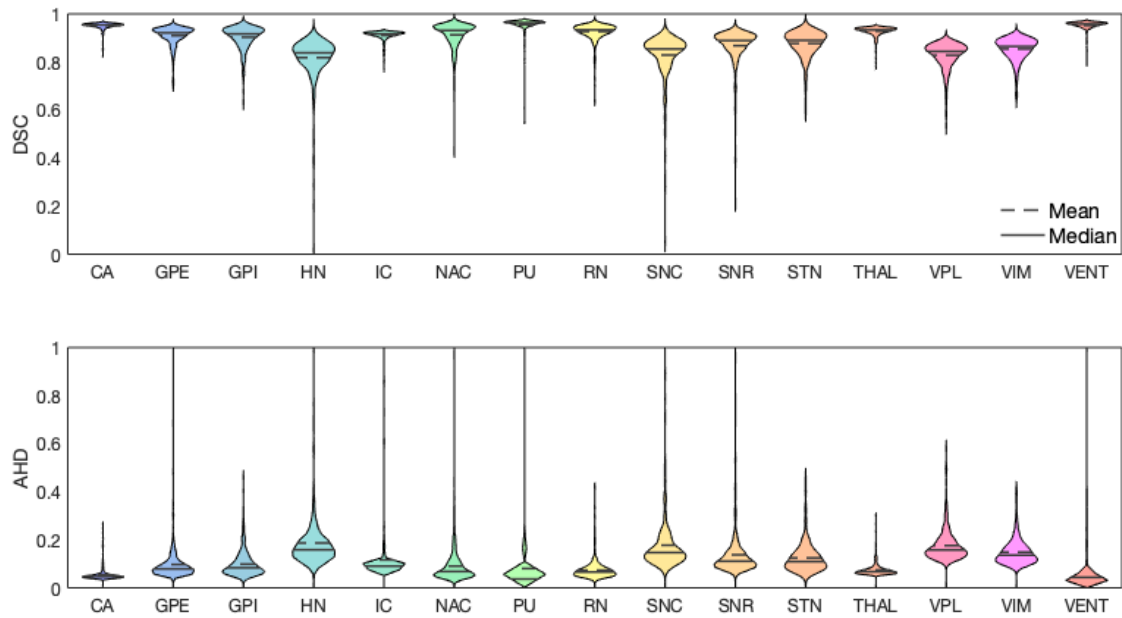


Figure S10: **The external tests performance on each label.** On the top, the DSC of each label was measured for all the external test subjects. For each subject, the DSC value was measured separately for the left and the right hemisphere, then averaged for the plot. Similarly, on the bottom, the AHD was measured. The full name of the labels can be find in table S3.

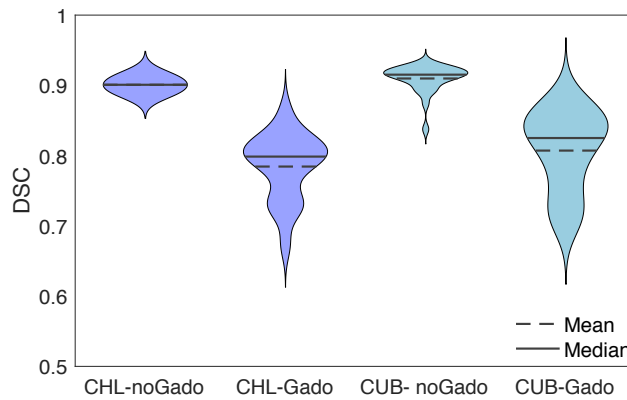


Figure S11: **Comparison of the gadolinium enhanced and non-gadolinium enhanced scans in the CHL and CUB dataset.** Among the CHL data, 18 out 20, and among the CUB, 13 out of 39 were gadolinium enhanced.

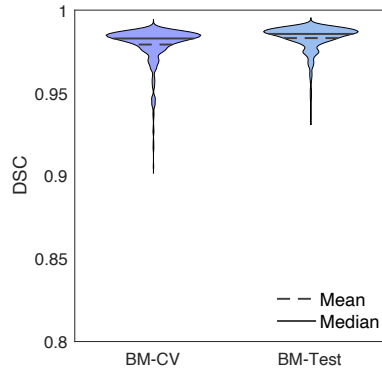


Figure S12: **The DSC between the network and the gold standard brain mask.** The DSC is plotted for all the cross-validation subjects (BM-CV), and all the test subjects (BM-Test).

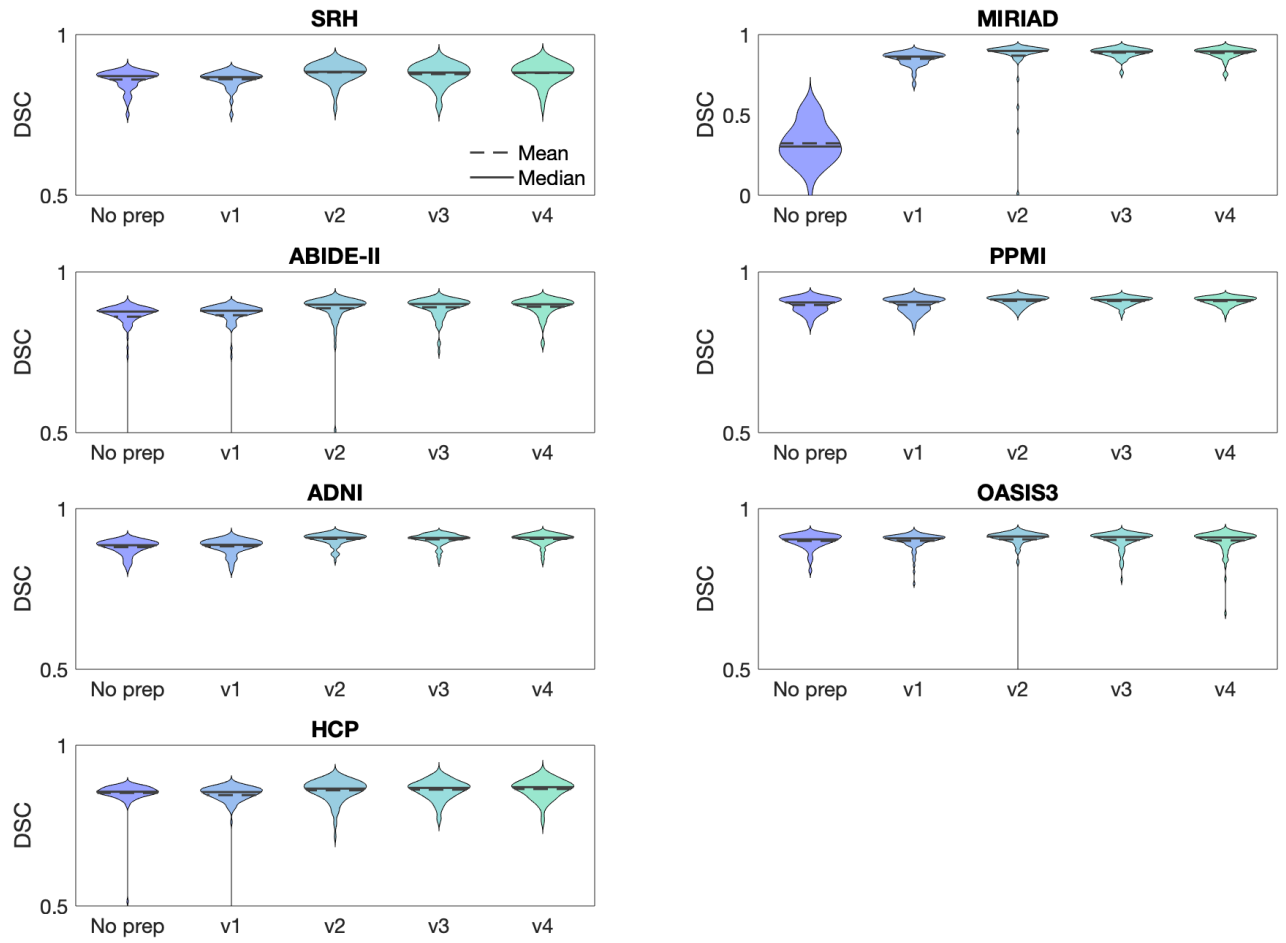


Figure S13: **Ablation Study on the pre-processing separately on each LODO cross-validation dataset.**

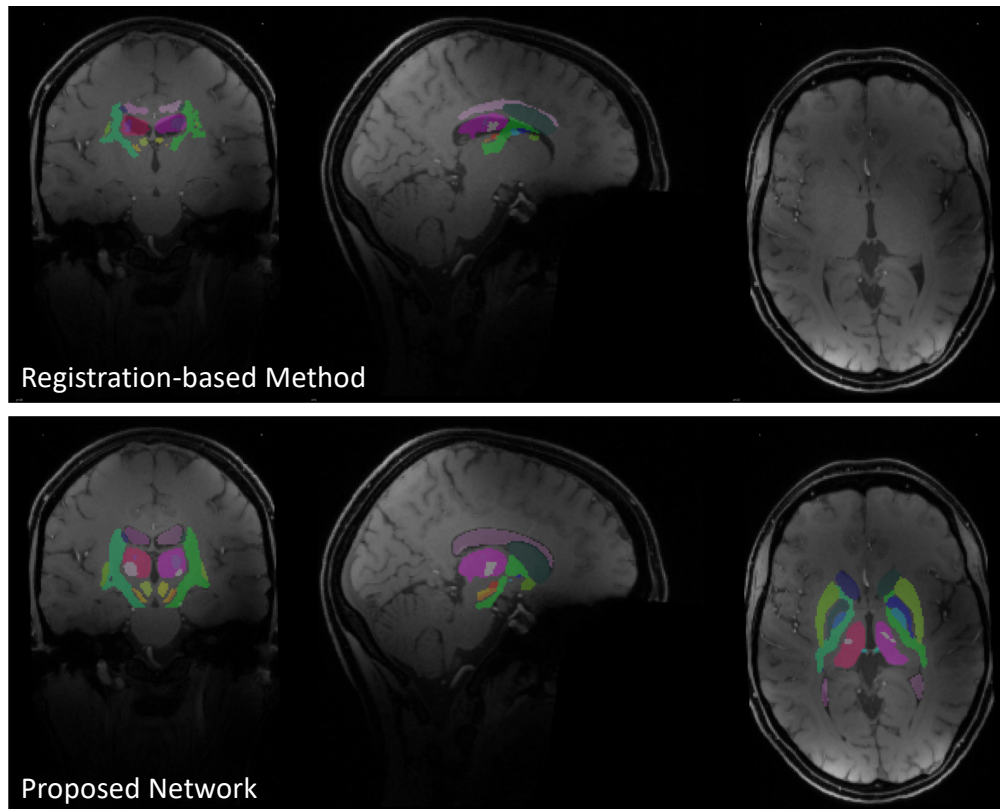


Figure S14: The result of the deep brain structures segmentation by the proposed network and registration-based method a 7T MRI scan.

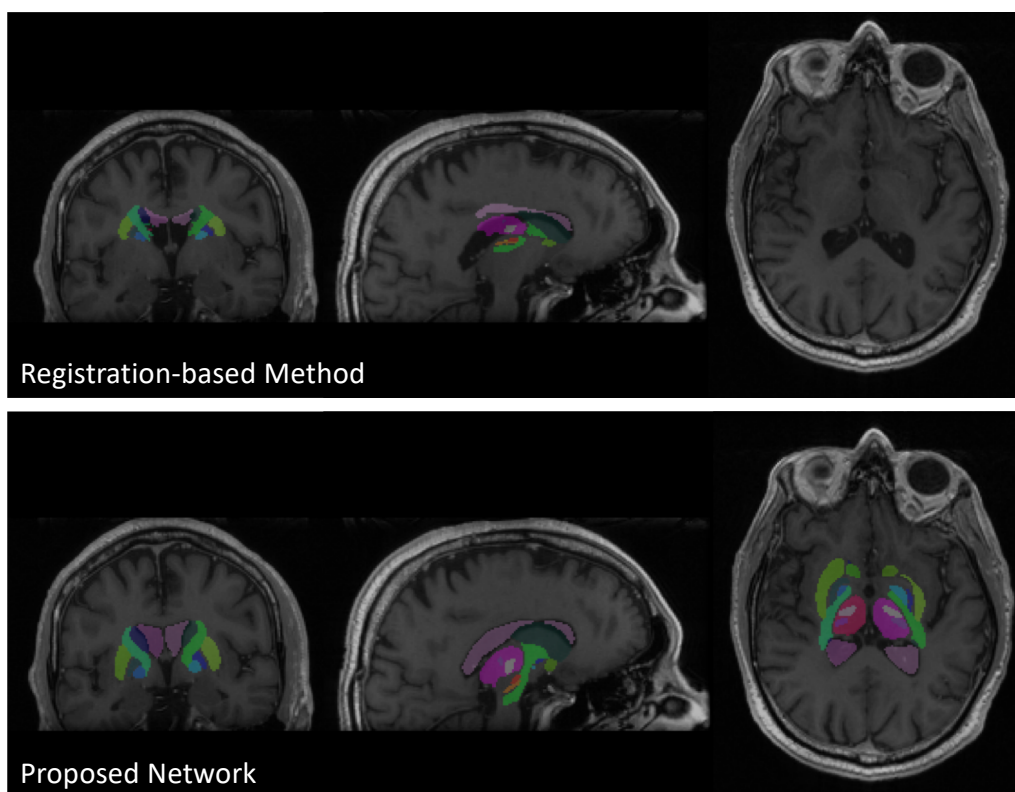


Figure S15: The result of the deep brain structures segmentation by the proposed network and registration-based method on an incomplete MRI scan.

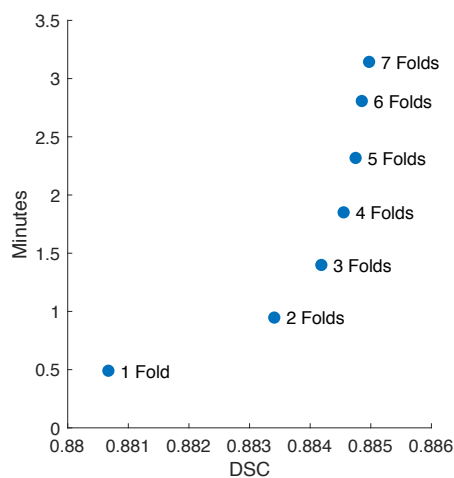


Figure S16: Comparison of the inference time and the DSC of the performance when using different number of folds (networks) for the ensemble. The network performance was compared to the registration-based method. For each number of folds, all the possible combinations were considered, 7, 21, 36, 36, 21, 7, 1 combinations for 1, 2, 3, 4, 5, 6, and 7 folds. The average performance among the possible combinations are shown in this plot.